

Break through the Steric Hindrance of Ionic Liquids with Carbon Quantum Dots to Achieve Efficient and Stable Perovskite Solar Cells

Shaohua Chi, Shuo Yang, Yijie Wang, Dan Li, Le Zhang, Lin Fan, Fengyou Wang, Xiaoyan Liu, Huilian Liu, Maobin Wei, Jinghai Yang* and Lili Yang*



Cite This: *ACS Appl. Mater. Interfaces* 2023, 15, 48304–48315



Read Online

ACCESS |

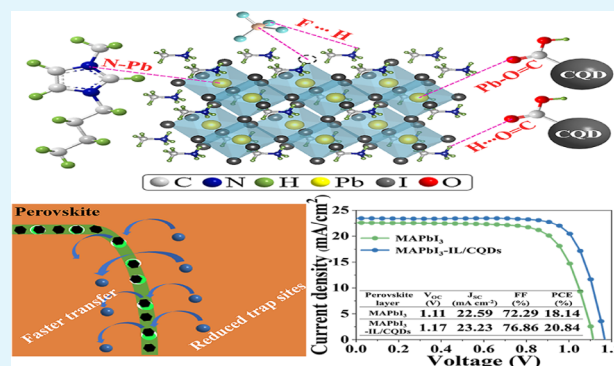
Metrics & More

Article Recommendations

Supporting Information

ABSTRACT: Overcoming the negative impact of residual ionic liquids (ILs) on perovskite films based on an in-depth understanding of chemical interactions between ionic liquids and preparing perovskite precursor solutions is a great challenge when aiming to simultaneously achieve long-term stability and high efficiency within IL-based perovskite solar cells (PSCs). Herein, 1-butyl-3-methylimidazolium tetrafluoroborate (BMIMBF₄), a type of IL, was introduced into the perovskite precursor solution, and carbon quantum dots (CQDs) were further introduced into the antisolvent to enhance the photovoltaic properties of PSCs. Both ILs and CQDs synergistically manipulate the crystallization process and passivate defects to obtain high-quality perovskite films. Besides serving as passivation sites to strengthen the collaboration between additives and perovskite materials, the cointroduction of CQDs further promotes the carrier transport process since it not only provides carrier channels at grain boundaries but also forms better energy alignment, which effectively overcomes the charge transfer loss caused by the steric hindrance of ILs. Based on such a synergistic effect of ILs and CQDs, the n-i-p MAPbI₃-based PSCs achieve the highest efficiency of 20.84% with improved stability. This simple and low-cost synergistic integration method will subsequently provide direction for optimizing ILs to improve the photovoltaic performance of PSCs.

KEYWORDS: photovoltaic performance, synergistic effect, defect passivation, charge transport properties, ionic liquid



1. INTRODUCTION

The outstanding optoelectronic characteristics exhibited by perovskite materials have fueled a surge in research on perovskite solar cells (PSCs), positioning them as one of the most promising photovoltaic technologies.^{1,2} Although PSCs have reached a maximum certified power conversion efficiency (PCE) of 25.8%, their successful commercialization still lacks reliable long-term stability.^{3–6} Generally speaking, the recognized reasons for the rapid PCE decline are ascribed to the self-decomposition caused by water and oxygen molecules penetrating into the perovskite grain gap, ion migration along the grain boundary, etc.^{7,8} The issues caused by water and oxygen can be solved by encapsulation technology, while the ion migration cannot be synchronously solved since it originates from the characteristics of perovskite materials themselves.^{9,10} The lower activation energies of organic and halide ions make them tend to transition from the lattice to the grain boundary (GB) or interface in response to external stimulation, which can cause serious self-doping effects and collapsing of the perovskite structure. Obviously, the good encapsulation of hybrid perovskite materials cannot prevent such an intrinsic ion migration phenomenon.^{2,11–13} Hence, inhibiting ion migration in PSCs is crucial to achieving both

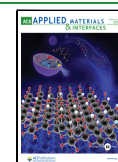
high efficiency and guaranteeing stability during operational conditions.

Recently, environmental-friendly ionic liquids (ILs) have been used as additions in precursor solutions to allow the perovskite films to resist ion migration.^{14–17} Since Snaith et al. added large molecular ILs of 1-butyl-3-methylimidazolium tetrafluoroborate (BMIMBF₄) into the perovskite precursor solutions and significantly enhanced both the device's characteristics and its long-term stability in 2018, different kinds of ILs such as small molecular, macromolecular imidazolium, and macromolecular pyridine have been applied into PSCs.^{18–20} Among them, the ILs of macromolecular imidazolium have attracted great attention since the unique properties of low vapor pressure, high viscosity, and strong polarity can provide a good liquid region between perovskite grains and advantageously regulate high-quality perovskite

Received: August 2, 2023

Accepted: September 22, 2023

Published: October 4, 2023



growth, which have been also proved to possess the ability to interact with the perovskite precursor solution through chelation and hydrogen bonding to inhibit ion transfer.^{21–25}

While the ILs may enhance interaction with the perovskite precursor and potentially function as either electron acceptors or donors, they can also form adducts with the additive rather than forming complexes with the solvent.²¹ It has been reported that the ILs cannot be volatilized after high-temperature annealing due to their low vapor pressure, and hence, a certain amount of ILs remain in the as-deposited perovskite, forming a low-dimensional complex with PbI_2 .^{18,26,27} Due to the low conductivity of such a low-dimensional complex, the steric hindrance effect will appear, which may in turn adversely affect the charge separation and transport processes, and even result in energy band mismatch between the perovskite film and the transport layer.^{18,20} Thus, even though the stability of a PSC can be improved by using ILs as additives, its efficiency is usually sacrificed. To overcome this issue, Chen et al. recently used hydrochloric acid (HCl) to make the methylammonium acetate (MAAc) ionic liquid escape from the perovskite film by a substitution reaction.²⁸ However, this method is not suitable for large molecular ILs with more passivation sites. Therefore, as for the macromolecular imidazolium ILs, developing efficient charge transport channels at the grain boundaries to reduce the steric hindrance effect proved to be a promising approach for overcoming the limitations of ILs, leading to achieving both efficient and stable PSCs.

Selecting appropriate high-conductive inorganic materials to construct a charge transfer channel at perovskite grain boundaries is a promising approach to reduce the steric hindrance effect of polymers, promote charge transport across grain boundaries, and achieve higher PCE in PSCs.^{29–31} Carbon quantum dots (CQDs) have been proven to possess great advantages such as a large absorption coefficient,³² a wide absorption spectrum, and good photoinduced electron transfer/charge separation ability,³³ which is essential in photovoltaic applications since they can effectively transfer electrons and prevent the recombination of electron–hole pairs.^{34,35} Moreover, they can also participate in the perovskite growth process to delay the crystal growth rate of perovskite grains.^{36–39} Therefore, if we combine the CQDs and ILs to co-optimize the perovskite film, the following advantages can be realized: (1) both CQDs and ILs have diversified passivation sites to coordinate with Pb-related defects, leading to enhancements in the crystal quality of perovskite films; (2) carbon quantum dots can anchor at the grain boundary of perovskite to serve as carrier transport channels; and (3) the band alignment of devices can be further tuned to achieve a much better matching status. Thus, we can expect that this strategy can achieve the purpose of simultaneously enhancing device efficiency and improving stability.

Herein, we developed a simple and low-cost molecule targeted anchoring grain boundary (TAGB) strategy via synergistic effects between zero-dimensional material CQDs and macromolecular imidazolium ILs BMIMBF₄. In detail, as illustrated in Scheme S1 (Supporting Information), ILs were incorporated into the perovskite precursor solution and CQDs were introduced into perovskite films via a chlorobenzene (CB) antisolvent process. The synergistic effects of BMIMBF₄ and CQDs additives on perovskite films and devices were systematically studied. The cointroduction of CQDs further strengthens the interaction between additives and the perov-

skite and promotes the carrier transport process since CQDs not only serve as passivation sites but also provide carrier channels at grain boundaries. Thereby, besides exerting the role of ionic liquids in inhibiting ion migration to improve the stability, it is also conducive to solving the hindrance effect caused by macromolecular ILs to some extent to enhance the PCE of PSCs. Therefore, with exceptional stability, we ultimately achieved a maximum PCE of 20.87%, which is the champion PCE of large-molecule IL-based MAPbI₃ n-i-p PSCs to the best of our knowledge (Table S1).

2. MATERIALS AND METHODS

2.1. Materials. All of the materials and reagents were used as received without any purification. Lead iodide (PbI_2), methylammonium iodide (MAI), SnO_2 (15% in a water colloidal dispersion), and chlorobenzene (CB) were purchased from Sigma-Aldrich. ITO-coated glass substrate, Spiro-OMeTAD, and all anhydrous solvents were obtained from YOUXUAN Tech (China). Carbon quantum dots (CQDs) and 1-butyl-3-methylimidazolium tetrafluoroborate (BMIMBF₄) were purchased from Beijing Beida Jubang Technology Co., Ltd. and Aladdin Shanghai, respectively.

2.2. Preparation of Perovskite Precursor Solutions. We prepared the MAPbI₃ perovskite precursor solution using 463 mg of PbI_2 and 162 mg of MAI in 1 mL of *N,N*-dimethylformamide (DMF)/dimethyl sulfoxide (DMSO) (7/3) mixed solvents. For the perovskite precursor solution containing BMIMBF₄, we added BMIMBF₄ with a lead atom ratio of 0.2–0.5 mol % to the perovskite precursor. Blending and filtering (0.45 μm , PTFE) were performed in a glovebox before use.

2.3. Preparation of Antisolvent. 1 mg of CQD was dissolved by 20, 10, 7, and 5 mL of CB, separately. That is, the concentration of CQDs can be determined to be 0.05, 0.1, 0.15, and 0.2 mg mL^{-1} , respectively.

2.4. Synthesis of Perovskite Films. The ITO glass substrates underwent a 20 min sonication process sequentially with deionized water, ethyl alcohol, acetone, and ethyl alcohol, followed by a 20 min treatment under ultraviolet (UV)-ozone. The SnO_2 precursor solution was prepared through a 12 h stirring of the SnO_2 colloidal dispersion with deionized (DI) water at a 1:1 volume ratio. Subsequently, the SnO_2 was spin-coated onto the ITO substrates at 5000 rpm for 30 s, and the resulting electron transport layers (ETLs) were obtained by annealing on a hot plate at 150 °C for 30 min in an ambient atmosphere.

The process began by transferring the ITO/ SnO_2 substrates into a nitrogen-filled glovebox to facilitate the deposition of the perovskite film. Next, 85 μL of the MAPbI₃ precursor solution was dipped at 4500 rpm for 35 s on the SnO_2 substrates. At the 18 s mark after starting this procedure, 350 μL of antisolvent was gently poured onto the rotating substrate. The resulting film was subsequently annealed at 60 °C for 5 min and then at 100 °C for 10 min to yield the perovskite film. It is worth noting that the entire perovskite film fabrication process occurred within a controlled nitrogen environment in the glovebox. We named the film produced using the IL “MAPbI₃-IL” and the film created using IL/CQDs “MAPbI₃-IL/CQDs”.

2.5. Device Fabrication. The preparation of hole transport layers (HTLs) involves the following steps. First, a mixture was created by combining 72 mg of Spiro-OMeTAD with 29 μL of a solution containing 550 mg mL^{-1} Li-TFSI in acetonitrile, along with 19 μL of 4-*tert*-butylpyridine in 1 mL of chlorobenzene (CB). Subsequently, 70 μL of this mixture solution was applied onto the previously prepared MAPbI₃ films by using a spin-coating process at 3000 rpm for 35 s. Lastly, a 100 nm-thick layer of Ag was deposited under vacuum conditions.

3. RESULTS AND DISCUSSION

In order to enhance the concentration of the BMIMBF₄ additive, various perovskite thin films deposited on SnO_2 /ITO substrates were prepared by adding 0–0.5 mol % (relative

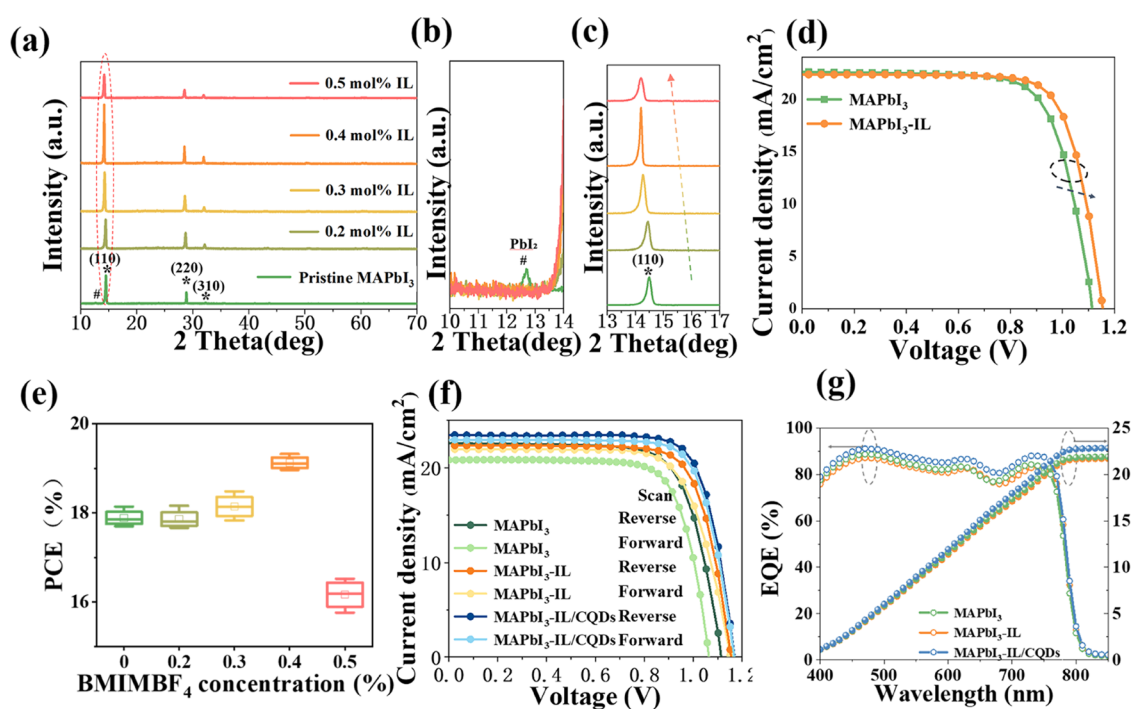


Figure 1. (a) XRD patterns of perovskite films treated with different IL concentrations. (b) Enlarged XRD patterns of (110) diffraction peaks. (c) Enlarged diffraction profile of PbI_2 in the range of 10–14°. (d) J – V curves of perovskite devices treated with and without 0.4 mol % IL. (e) Statistical results of the PCE for the devices without and with different amounts of ILs. (f) Forward-scan and reverse-scan J – V curves of champion MAPbI_3 , MAPbI_3 –IL, and MAPbI_3 –IL/CQDs-based PSCs. (g) EQE spectra and integrated current curves.

to lead atoms) BMIMBF_4 into the precursor solution, which were named 0.2 mol % IL, 0.3 mol % IL, 0.4 mol % IL, and 0.5 mol % IL. To evaluate the efficacy of BMIMBF_4 on the crystalline properties of perovskite films, X-ray diffraction (XRD) patterns are initially captured. As shown in Figure 1a, the formation of the tetragonal perovskite phase is indicated by the presence of characteristic XRD peaks at 14.4, 28.7, and 32.1°, which correspond to the crystal planes of (110), (220), and (310), respectively. Figure S1 shows the variation in the intensity and fwhm (full width at half-maximum) of the (110) diffraction peak as the concentration of BMIMBF_4 increases. At 0.4 mol %, the intensity reaches its maximum value and fwhm reaches its minimum value, indicating that the crystal quality is optimal at this concentration. However, when we further increase the BMIMBF_4 concentration to 0.5 mol %, the crystal quality turns worse again. This is mainly because excessive ILs can lead to higher viscosity in the precursor solution, which may affect the intermediates in the perovskite precursor.⁴⁰ Moreover, as shown in the enlarged XRD patterns in Figure 1b, a weak diffraction peak appears at 12.7° in the MAPbI_3 perovskite films. This can be attributed to PbI_2 .⁴¹ With the addition of BMIMBF_4 , the signal of PbI_2 disappeared, suggesting that the crystallization of perovskite has been improved. As shown in Figure 1c, the XRD peak shifts to a small angle via adding ILs, implying the potential incorporation of BMIMBF_4 molecules into the perovskite crystal lattice.^{42,43} Therefore, the best MAPbI_3 –IL perovskite films with less defect density and higher crystallinity have been achieved when the concentration of BMIMBF_4 is 0.4 mol %.

Subsequently, a series of PSCs based on 0.2 mol % IL, 0.3 mol % IL, 0.4 mol % IL, and 0.5 mol % IL perovskite films with the n-i-p structure of ITO/ SnO_2 / MAPbI_3 /Spiro-OMeTAD/Ag are fabricated. Figure S2 displays the corresponding J – V curves, while Table S2 presents the statistical key photovoltaic

parameters with varying amounts of ILs. Obviously, the variation tendency of PCE via IL adding an amount exhibits good agreement with the XRD results. Furthermore, a bunch of 20 devices for each adding amount of ILs has been fabricated, and the corresponding statistical distribution image of PCE has been illustrated in Figure 1e, clearly proving the repeatability of effects of ILs on the photovoltaic performance of PSCs. Regarding the MAPbI_3 PSCs, they initially demonstrated a low V_{OC} of 1.11 V, a J_{SC} of 22.59 mA cm^{-2} , and an FF of 72.29%, leading to a PCE of 18.14%. However, upon introduction of BMIMBF_4 , the PCE of the optimized device increased to 19.32% for 0.4 mol % IL-based PSCs. This improvement was accompanied by a J_{SC} of 22.36 mA cm^{-2} , a V_{OC} of 1.15 V, and an impressive FF of 74.95%. Notably, even though the crystal quality of IL-based perovskite films improves, the J_{SC} in the corresponding PSCs exhibits a very slight decrease on the contrary. As previously reported, it is mainly attributed to the residual ILs gathering at the perovskite grain boundary, which prompts the formation of a complex between ionic liquids and lead iodide to increase the steric hindrance of devices and then hinder the charge transport.^{18,20,44}

To overcome the above issue, the CQDs were further introduced into the perovskite films via an antisolvent method. Figure S3a displays the transmission electron microscope (TEM) image and the diameter distribution of CQDs. Evidently, the CQDs exhibit a uniform size and a nearly spherical morphology. Statistical analysis of over 300 particles using ImageJ software determined that the average size of the CQDs is approximately 2.1 nm (Figure S3b). Furthermore, Figure S3c illustrates the UV–visible (UV–vis) absorption and steady-state photoluminescence (PL) spectra of CQDs in water. The absorption range of 300–400 nm originating from CQDs will improve the UV light utilization of PSCs. The PL

Table 1. Photovoltaic Parameters and Hysteresis Index of Champion MAPbI₃, MAPbI₃-IL, and MAPbI₃-IL/CQDs PSCs

perovskite layer	scan direction	V _{OC} (V)	J _{SC} (mA cm ⁻²)	FF (%)	PCE (%)	HI
MAPbI ₃	forward	1.09	21.06	72.07	16.54	0.08
	backward	1.11	22.59	72.29	18.14	
MAPbI ₃ -IL	forward	1.12	22.32	73.78	18.49	0.04
	backward	1.15	22.36	74.95	19.32	
MAPbI ₃ -IL/CQDs	forward	1.17	22.92	75.81	20.26	0.03
	backward	1.17	23.23	76.86	20.84	

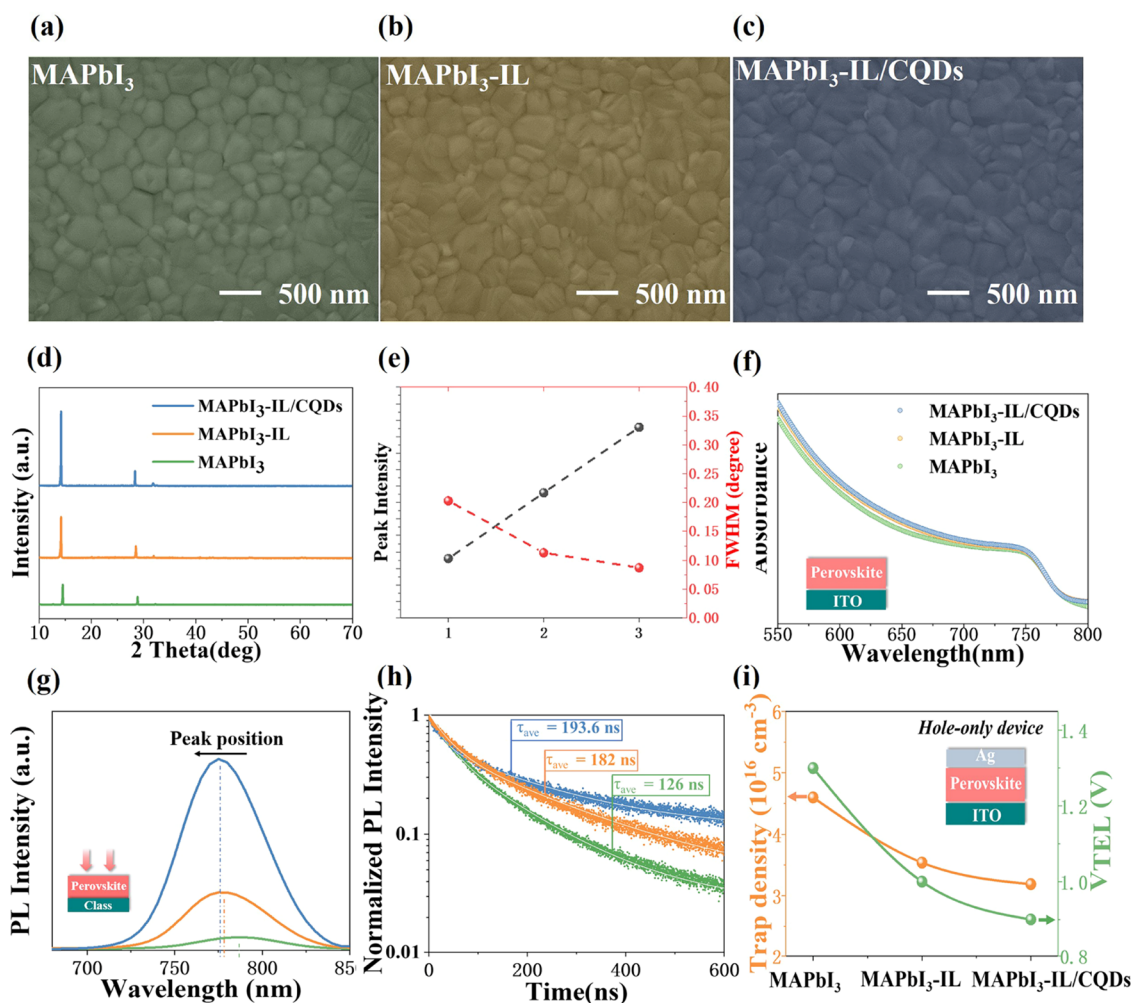


Figure 2. (a–c) Scanning electron microscopy (SEM) images of corresponding perovskite films with a scale of 500 nm. (d) XRD patterns of the respective films deposited on SnO₂/ITO substrates. (e) Peak intensity and fwhm variation of the (110) crystal plane for corresponding perovskite films. 1, MAPbI₃; 2, MAPbI₃-IL; and 3, MAPbI₃-IL/CQDs. (f) Absorption spectra pertaining to the respective films. (g) PL spectra and (h) TRPL spectra obtained from films deposited on glass substrates. (i) Trap density of corresponding films obtained from the SCLC method.

spectrum of CQDs aqueous solution (0.15 mg mL⁻¹) with 350 nm excitation exhibits an emission of 450 nm in blue color, indicating that CQDs can convert ultraviolet light into visible light to improve their light absorption capacity. Fourier transform infrared spectroscopy (FTIR) (Figure S3d) was used to identify the functional groups on the surface of CQDs. The characteristic peaks at 1080, 1709, and 3443 cm⁻¹ are related to the vibration of C–O, the stretching vibration of the C=O bond, and the vibration of OH, respectively, suggesting that a large number of carboxyl groups are functionalized on the surface of CQDs,^{38,39} which can serve as coordination sites for passivation defects to further improve the crystal quality of perovskite films.

Accordingly, a series of PSCs based on 0.4 mol % IL perovskite films by further adding different amounts of CQDs (0.05–0.20 mg mL⁻¹) with the architecture of ITO/SnO₂/MAPbI₃/Spiro-OMeTAD/Ag are fabricated. Figure S4 displays the *J*–*V* curves for the respective PSCs, while Table S3 provides a summary of the detailed photovoltaic parameters as a function of the CQD additive concentration. At a CQDs concentration of 0.15 mg mL⁻¹, the highest PCE of 20.84% was achieved with a *J*_{sc} of 23.23 mA cm⁻², a *V*_{oc} of 1.17 V, and an FF of 76.86. The obvious enhancement in each photovoltaic parameter of MAPbI₃-ILs/CQDs PSCs compared to those of MAPbI₃ PSCs and MAPbI₃-IL PSCs implies that CQDs make a positive contribution here and might form a synergistic effect with ILs. To further prove it, we presented the forward-scan

and reverse-scan J - V curves of optimized MAPbI₃ PSCs, MAPbI₃-IL PSCs, and MAPbI₃-IL/CQDs PSCs in Figure 1f to clearly see their difference. Their corresponding photovoltaic parameters are shown in Table 1. Figure 1e exhibits the corresponding external quantum efficiency (EQE) spectra and integral photocurrent curves. The obtained integrated photocurrents for MAPbI₃ PSCs, MAPbI₃-IL PSCs, and MAPbI₃-IL/CQDs PSCs are 22.34, 22.08, and 23.07 mA cm⁻², respectively, which is consistent with the J - V results. The hysteresis index (H-index) values were then calculated according to the equation $H\text{-index} = (\text{PCE}_{\text{Reverse}} - \text{PCE}_{\text{Forward}}) / \text{PCE}_{\text{Reverse}}$ to be 0.09, 0.04, and 0.003 for MAPbI₃, MAPbI₃-IL, and MAPbI₃-IL/CQDs PSCs, respectively. Generally, the hysteresis is usually ascribed to the ion movement, charge transfer imbalance, and accumulation at the interfaces.⁴⁵ The step using reduced hysteresis for MAPbI₃-IL PSCs and MAPbI₃-IL/CQDs PSCs further proves the positive synergistic effect of both additives on ion movement, charge transfer, and then device performance.

Figure 2a-c shows the scanning electron microscopy (SEM) images of MAPbI₃, MAPbI₃-IL, and MAPbI₃-IL/CQDs films to reveal the synergistic effect of ILs and CQDs on the perovskite surface morphology. Compared to the control sample, the introduction of IL/CQDs leads to a reduction in the formation of unfavorable pinholes in perovskite films, resulting in a more compact and homogeneous morphology. The grain size statistical distribution images in Figure S5 show that the average grain sizes are 224.1, 285.4, and 354.89 nm for MAPbI₃, MAPbI₃-IL, and MAPbI₃-IL/CQDs films, respectively. To unveil the crystal growth mechanism of gradually enlarged grain sizes, the color changes of the photos taken on the perovskite films during a 60 °C postannealing process are shown in Figure S6. Obviously, the crystallization process is gradually delayed by adding IL and IL/CQDs in contrast with MAPbI₃ films. The introduction of IL into the solvent system leads to an elevation in viscosity, consequently causing a reduction in the rate of solvent evaporation. This decrease in evaporation rate, in turn, leads to a diminished concentration increment, thereby resulting in a lower nucleation rate for MAPbI₃-IL films.^{45,46} Further addition of CQDs then makes further efforts to delay the crystallization process of perovskite films. Compared with the unannealed MAPbI₃ films, the XRD patterns of the unannealed MAPbI₃-IL and MAPbI₃-IL/CQDs films exhibited a greater presence of amorphous signals, thereby affirming the preceding discussion (Figure S7). Therefore, the best crystal quality can be achieved in MAPbI₃-IL/CQDs films.

XRD patterns were used to reveal the effect of mixed additives on the crystallization characteristics of the perovskite films. Figure 2d illustrates that the MAPbI₃-IL/CQDs films exhibit the highest diffraction intensity and the narrowest full width at half-maximum (fwhm) (Figure 2e), demonstrating that the mixed additives of ILs/CQDs indeed improve the crystallinity of perovskite films. Moreover, on further adding CQDs, the peak shift did not happen for the MAPbI₃-IL/CQDs films in comparison with that of the MAPbI₃-IL films, indicating that CQDs molecules failed to integrate into the perovskite crystal lattice, potentially resulting in their accumulation at the grain boundaries, which is consistent with previous reports that CQDs can passivate perovskite grain boundaries and provide nucleation sites.³⁹ In addition to the morphology and crystallization of perovskite films, the corresponding photophysical properties are also key factors

to achieve high photovoltaic performance within PSCs.^{9,47} Therefore, in Figure 2f, the absorption spectra of the corresponding films are depicted. In comparison to the MAPbI₃ films, one can readily observe a significant enhancement in absorption throughout nearly the entire visible-light range for both the MAPbI₃-IL films and MAPbI₃-IL/CQDs films. This enhancement can be attributed to the beneficial effects of additives on increasing grain size and improving crystal quality, as illustrated in Figure S5.

Meanwhile, the perovskite films were further studied by steady-state photoluminescence (PL) and time-resolved photoluminescence (TRPL) spectra. Similarly, as shown in Figure 2g, the MAPbI₃-IL/CQDs films possess the strongest PL intensity and an obvious blue shift in peak position compared to the MAPbI₃ films and MAPbI₃-IL films, once more proving that the synergistic effect of ILs and CQDs greatly improved the crystal quality and reduced the trap-state density within perovskite films. The TRPL decay curves in Figure 2h can be fitted by a biexponential decay function: $f(t) = A_1 \exp(-t/\tau_1) + A_2 \exp(-t/\tau_2)$, where A_1 and A_2 are the decay amplitudes and τ is the decay time constant. In general, the fast decay time of τ_1 can be attributed to the trap-assisted recombination, and the low decay time of τ_2 can be attributed to the radiation recombination of photogenerated carriers.⁴⁸ The fitted parameters are summarized in Table S4. As expected, the average charge lifetime (τ_{ave}) is greatly extended from the original 126 to 182 and 194 ns via sequentially introducing ILs and CQDs, confirming that ILs/CQDs strongly suppressed the trap-assisted recombination. In order to verify the suppression impact of IL/CQDs on defect density suppression, we conducted measurements of dark I - V curves using hole-only devices and the pulsed-voltage space charge-limited current (SCLC) technique. The pulsed voltage was applied with a 200 ms delay time, ranging from 0 to 3 V. Figure S8 illustrates the results, which exhibit three distinct regions corresponding to low bias (ohmic region), medium bias (trap-filled region), and high bias (SCLC region) voltages.⁴⁹ The trap-filled voltage (V_{TFL}) is defined as the voltage at the kink point between the ohmic region and the trap-filled region. This parameter enables the determination of the trap-state density (η_{trap}) using the following formula

$$\eta_{\text{trap}} = \frac{2\epsilon\epsilon_0 V_{\text{TFL}}}{qL^2} \quad (1)$$

where q is the elementary charge, L is the thickness of the perovskite film, ϵ is the relative vacuum permittivity of MAPbI₃ ($\epsilon = 28.8$), and ϵ_0 is the vacuum permittivity.⁵⁰ The calculated hole trap-state densities for the hole-only devices are as follows in Figure 2i: 4.60×10^{16} cm⁻³ for the MAPbI₃ film, 3.54×10^{16} cm⁻³ for the MAPbI₃-IL film, and 3.19×10^{16} cm⁻³ for MAPbI₃-IL/CQDs films. In addition, we also carried out a transient photovoltaic (TPV) test on the MAPbI₃, MAPbI₃-IL, and MAPbI₃-IL/CQDs PSCs (Figure S9). The results also show that the photovoltaic decay time of MAPbI₃-IL/CQDs PSCs is longer than that of MAPbI₃ and MAPbI₃-IL PSCs. The life prolongation further proves the effective trap passivation of IL/CQDs.^{47,48}

To explore the synergetic influence mechanism of ILs and CQDs on the crystal quality of perovskite films, we then studied the interaction between each additive and the perovskite precursor solution. The Fourier transform infrared spectroscopy (FTIR) spectra of pure IL, MAPbI₃ films, and

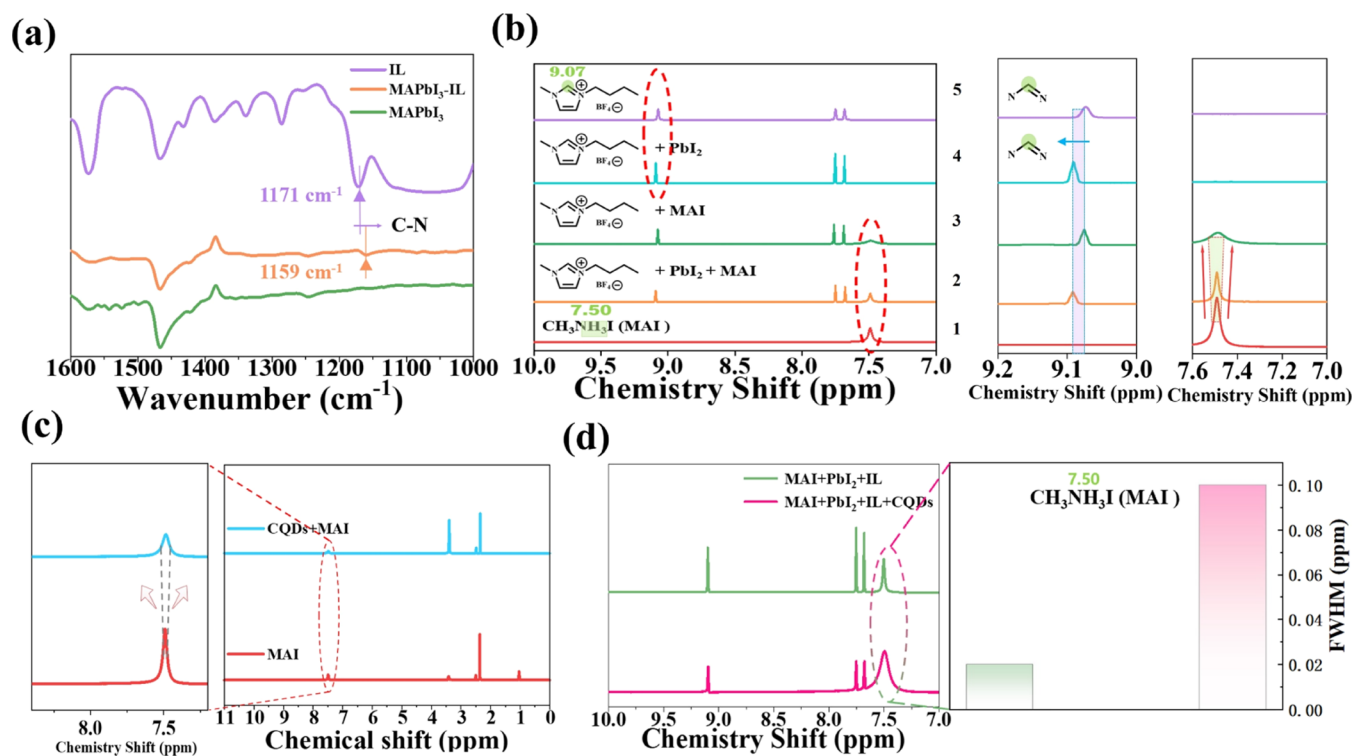


Figure 3. (a) FTIR spectra of IL, MAPbI₃ films, and MAPbI₃-IL films. (b) ¹H NMR spectra of IL, MAI, MAI + PbI₂ + IL, MAI + IL, and PbI₂ + IL. The corresponding H atoms of BMIMBF₄ and MAI that appeared in the spectra are highlighted as colored bars. (c) ¹H NMR spectra of MAI and CQDs + MAI and the enlarged region around 7.5 ppm. (d) ¹H NMR spectra of MAI + PbI₂ + IL and MAI + PbI₂ + IL + CQDs.

MAPbI₃-IL films are shown in Figure 3a. The stretching vibration peaks of C-N bonds detected at 1171 cm⁻¹ can be ascribed to the BMIMBF₄ liquid.^{40,46} It shifts to a lower wavenumber of 1159 cm⁻¹ in the MAPbI₃-IL films, indicating the presence of BMIMBF₄ within the perovskite films. The interaction between the perovskite precursor and ionic liquids (ILs) was examined by using ¹H nuclear magnetic resonance (¹H NMR) spectroscopy. Figure 3b illustrates that upon the addition of ILs to solutions containing PbI₂, MAI, and PbI₂-MAI in DMSO-d₆, the ¹H NMR signal of the C-N bond within ILs located at 9.07 ppm shows an obvious downfield shift. The largest peak shift happened in the ILs-PbI₂ solution, which demonstrated that the imidazole group of ILs forms a complex with PbI₂ through the interaction of a Pb-N coordination bond. The FTIR spectra of the pure IL and IL-PbI₂ are shown in Figure S10. Notably, after the addition of PbI₂ to the pure IL, the C-N stretching vibration of the IL shifts to the right. This is attributed to the interaction between the nitrogen atoms in IL and Pb.⁴⁶ Meanwhile, the sharp single ¹H NMR peak of MA⁺ locates at 7.50 ppm in MAI.⁵¹ It becomes broader in ILs-MAI and ILs-MAI-PbI₂ solutions (Figure 3b), and the width of the peak in the ILs-MAI solution is wider than that in ILs-MAI-PbI₂. Meanwhile, as for the ¹H NMR peak of the imidazole group within the IL, no shift appeared for pure MAI + IL solutions compared to that of pure IL, indicating that it should be the BF₄⁻ to interact with the MA⁺ cations by forming a hydrogen bond. In summary, the formation of strong coordination between the imidazole group and Pb²⁺ and the reinforcement of hydrogen bonding between BF₄⁻ and MA⁺ in the solution phase hinder the creation of MA⁺ or I⁻ vacancies and metallic Pb clusters. Moreover, they aid in retaining more MAI within the system to prevent its loss during the fabrication and annealing stages, which are essential

for maintaining a balanced reaction with PbI₂. These multiple benefits contribute to the production of high-quality perovskite films characterized by minimal trap density and the suppression of ion migration.

Similarly, the interaction between CQDs and perovskite precursors in solution was also characterized by ¹H NMR. As shown in Figure 3c, compared with the pure MAI, the characteristic peak of MAI broadens when the CQDs are mixed into the MAI solution, indicating that MA⁺ interacts with the carboxyl group by forming a typical hydrogen bond.⁶ Based on the above discussion results, we further investigate the interaction between the mixed additives of IL/CQDs and the perovskite precursor by ¹H NMR. Figure 3d presents the ¹H NMR spectra of IL alone and IL/CQDs with a perovskite precursor. When IL and CQDs are simultaneously added to the perovskite precursor solution, the ¹H NMR peak of MA⁺ turns wider than that of adding IL alone, indicating that a synergistic effect happened here, that is, MA⁺ interacts with both the carboxyl group in CQDs and BF₄⁻ within ILs.

The elemental compositions of the prepared perovskite samples were further characterized by X-ray photoelectron spectroscopy (XPS). In Figure S11a, we can observe that the Pb 4f spectrum of the MAPbI₃ perovskite films displays two distinctive peaks at 138.4 and 143.2 eV. These peaks correspond to the spin-orbit splitting of the Pb 4f_{7/2} and Pb 4f_{5/2} components, respectively.^{52,53} As for the MAPbI₃-IL and MAPbI₃-IL/CQDs films, the Pb 4f peak of MAPbI₃-IL films gradually shifts to a lower binding energy, which indicates a gradual increase in the electron cloud density of Pb atoms, proving the coordination between the ILs and the uncoordinated Pb²⁺ defects. Additionally, the further introduction of CQDs can enhance the coordination ability to Pb²⁺ defects. In addition, no change in the binding energy was detected in I 3d

XPS spectra. In conclusion, we presented a schematic of the mechanism for multiple passivation of defects by the hybrid additive (Figure 4).

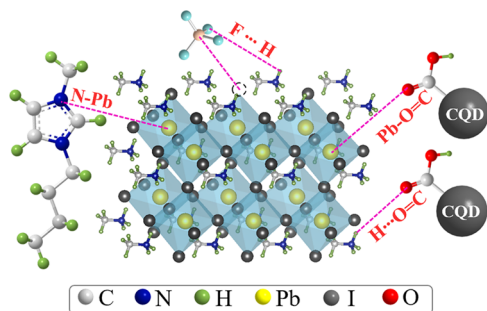


Figure 4. Schematic illustration of the interactions between IL and Pb^{2+} (N–Pb) through the cationic imidazole group, the hydrogen bonding between IL and MA^+ through the anionic BF_4^- , the interactions between CQDs and Pb^{2+} (O = C–Pb) through the carbonyl group, and the hydrogen bonding between CQDs and MA^+ through the carbonyl group.

To further explore the interfacial charge transfer dynamics between the perovskite films and charge transport layers, steady-state PL and time-resolved PL (TRPL) measurements were executed. Figure 5a shows the PL spectra of the $\text{SnO}_2/\text{MAPbI}_3$, $\text{SnO}_2/\text{MAPbI}_3\text{-IL}$ and $\text{SnO}_2/\text{MAPbI}_3\text{-IL/CQDs}$ films. Unsurprisingly, compared to the $\text{SnO}_2/\text{perovskite}$ films, there was no significant PL quenching observed in the $\text{SnO}_2/\text{MAPbI}_3\text{-IL}$ films, which was attributed to the poor conductivity of the polymers generated by ILs. After modification by IL/CQDs mixed additives, an obvious

quenching happened, indicating an enhanced electron extraction process between the perovskite and SnO_2 . Such a PL quenching effect can be confirmed by the lifetime variation tendency of the TRPL spectra shown in Figure 5b. An obviously decreased average carrier lifetime is obtained in the $\text{SnO}_2/\text{MAPbI}_3\text{-IL/CQDs}$ films, suggesting that the electron extraction property is improved. Moreover, as shown in Figure 5c,d, similar phenomena happen in the PL and TRPL spectra of $\text{MAPbI}_3/\text{Spiro-OMeTAD}$, $\text{MAPbI}_3\text{-IL/Spiro-OMeTAD}$, and $\text{MAPbI}_3\text{-IL/CQDs/Spiro-OMeTAD}$ samples. With IL/CQDs treatment, an accelerated photoinduced hole transfer from the perovskite to Spiro-OMeTAD is suggested by this observation. As a result, both efficient electron and hole collection processes are responsible for the improved J_{SC} .

To gain a deeper comprehension of the interface dynamics of PSCs, we conducted electrical impedance spectroscopy (EIS) measurements at open-circuit voltage under dark conditions. Figure S12 shows the EIS spectra of MAPbI_3 , $\text{MAPbI}_3\text{-IL}$, and $\text{MAPbI}_3\text{-IL/CQDs}$ PSCs, and the fitting parameters are shown in Table S5. Compared with MAPbI_3 PSCs, $\text{MAPbI}_3\text{-IL}$ PSCs exhibit a larger charge recombination resistance (R_{rec}), which indicates that the carrier recombination is reduced, resulting in the increased FF and V_{OC} . However, $\text{MAPbI}_3\text{-IL}$ PSCs exhibit a large charge transfer resistance (R_{ct}), which further indicates that the residual organic macromolecules hinder charge transport and reduce the J_{sc} . Notably, we found that $\text{MAPbI}_3\text{-IL/CQDs}$ PSCs exhibit the largest R_{rec} and the lowest R_{ct} . These results indicate that the synergistic effect of the mixed additive ILs/CQDs overcomes the drawbacks of the additive of BMIMBF_4 , further proving that the CQDs provide a carrier transport channel at the grain boundary and reduce the steric hindrance (Figure 6). Such

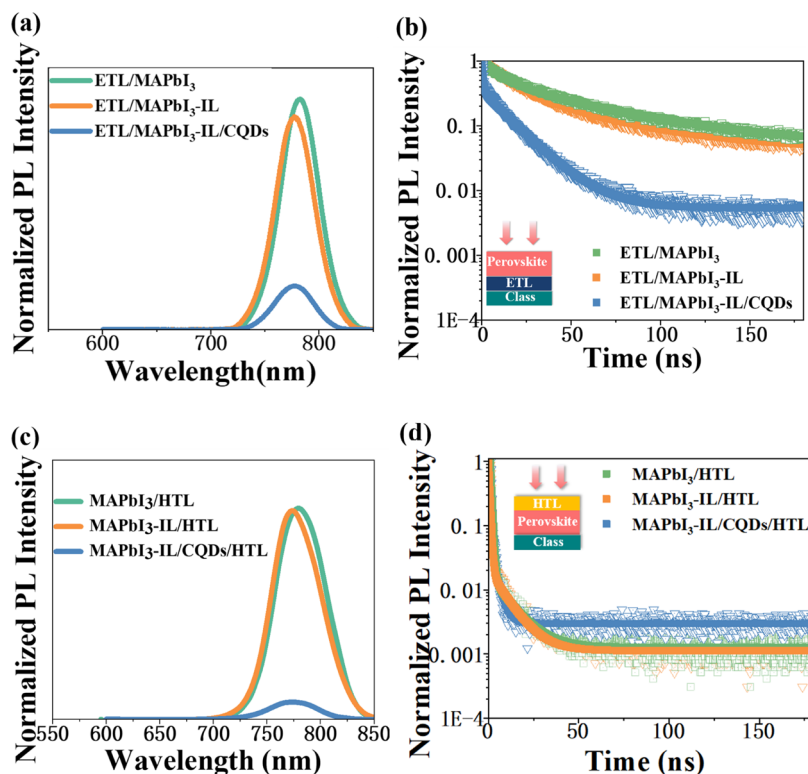


Figure 5. (a) Steady-state PL spectra and (b) TRPL spectra of perovskite films on SnO_2 . (c) Steady-state PL spectra and (d) TRPL spectra of perovskite films covered by Spiro-OMeTAD.

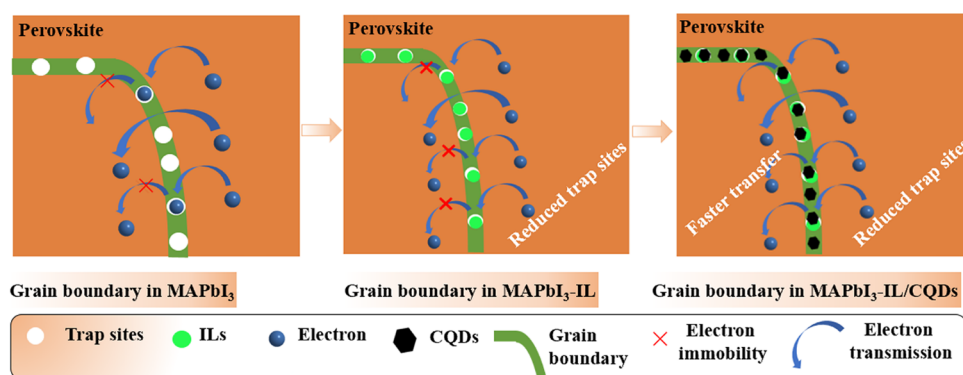


Figure 6. Schematic of recombination reduction by IL or IL/CQDs passivation.

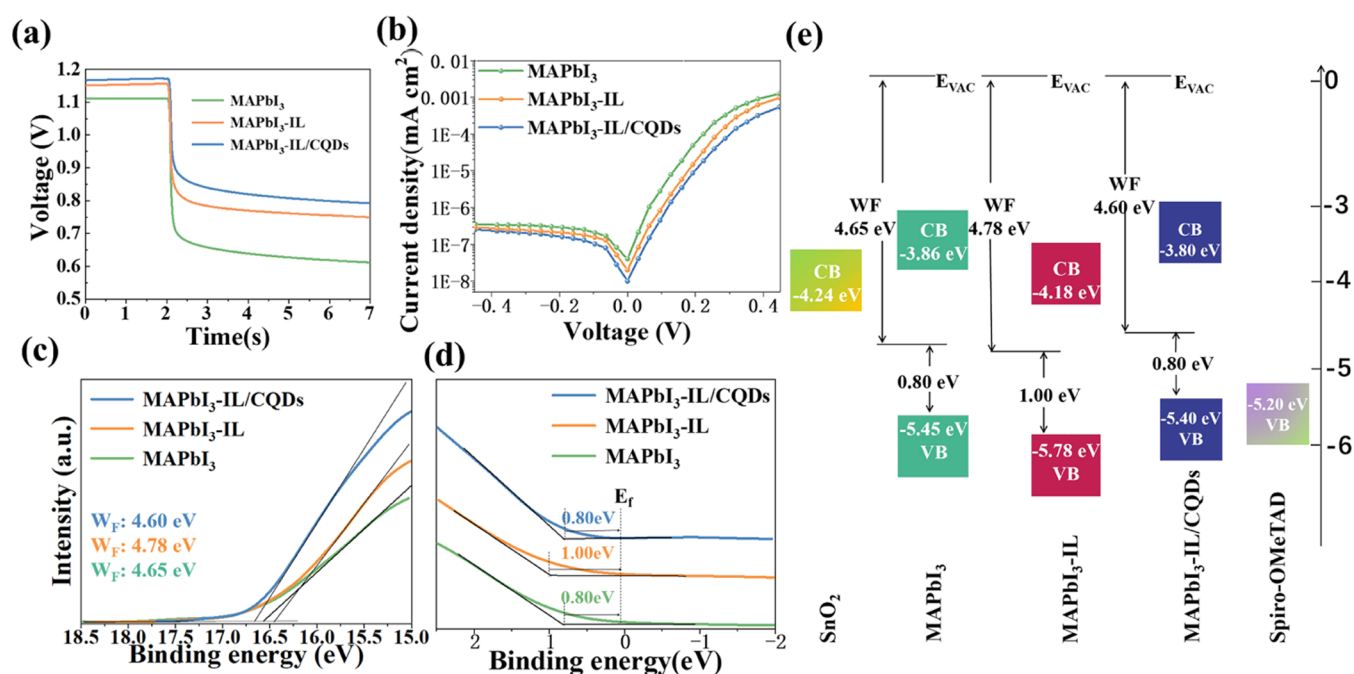


Figure 7. (a) OCVD curves. (b) J - V curves under the dark condition. (c) Cutoff region and (d) onset edge of UPS spectra of MAPbI₃, MAPbI₃-IL, and MAPbI₃-IL/CQDs films. (e) Energy band diagram of PSCs based on MAPbI₃, MAPbI₃-IL, and MAPbI₃-IL/CQDs films.

results are consistent with the smallest hysteresis for MAPbI₃-IL/CQDs PSCs (Figure 2a).

To prove the above results, we then characterize the open-circuit photovoltaic attenuation (OCVD) curves of MAPbI₃, MAPbI₃-IL-, and MAPbI₃-IL/CQDs-based devices. In Figure 7a, the OCVD measurements are depicted, providing insights into the carrier recombination process. The high voltage area and the index change area offer a means to comprehend this process. The MAPbI₃-IL/CQDs PSC exhibits a higher V_{OC} value and a more gradual decay in V_{OC} , indicating a reduced carrier recombination rate and an extended carrier lifetime, and evidencing that the recombination loss in the MAPbI₃-IL/CQDs PSC is suppressed. In addition, Figure 7b shows the corresponding dark J - V curves. The leakage currents of MAPbI₃-IL and MAPbI₃-IL/CQDs PSCs decrease gradually compared to the control device, which also indicates that the nonradiative recombination process in these devices has been suppressed.

The dynamics of charge transfer is also dependent on the energy-level structure of the device.^{54,55} The estimation of the conduction band minimum (CBM) and valence band

maximum (VBM) for the MAPbI₃ films, MAPbI₃-IL films, and MAPbI₃-IL/CQDs films was deduced from the ultraviolet photoemission spectroscopy (UPS) spectra and band gap energy, as depicted in Figures 7c-e and S13. Specifically, the CBM for the MAPbI₃ films was estimated to be -3.86 eV, with a corresponding VBM of -5.45 eV. In the case of the MAPbI₃-IL films, the CBM was estimated to be -4.18 eV, while the VBM was calculated to be -5.78 eV. Similarly, for the MAPbI₃-IL/CQDs films, the CBM and VBM were estimated at -3.90 and -5.50 eV, respectively. Obviously, the MAPbI₃-IL films form an unfavorable energy-level alignment at the interface, which can be attributed to the presence of highly electronegative BF₄⁻ anions on the surface of the MAPbI₃-IL films (Figure S14). It is well-known that the deposition of acceptor materials with strong electronegative characteristics on the surface of films can cause partial electron transfer, increase or create dipoles, and increase the work function (W_F), VBM, and CBM.⁵⁶ Therefore, the MAPbI₃-IL films hinder the transport of charge carriers, ultimately leading to a decrease in the device efficiency of the J_{sc} (Figure 1d). Compared to MAPbI₃-IL films, the MAPbI₃-IL/CQDs films

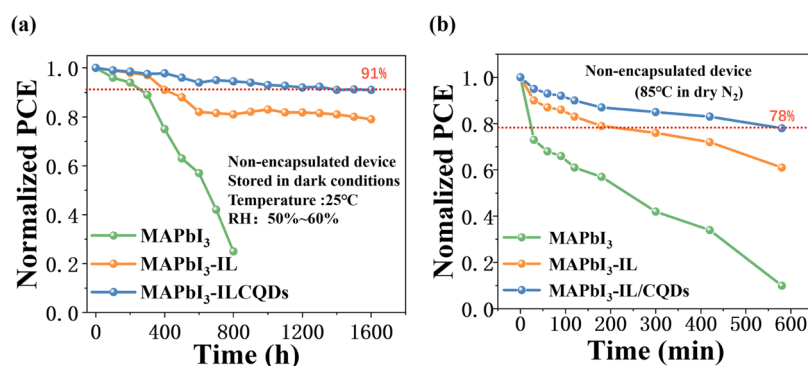


Figure 8. Normalized efficiency variation curves (a) under 50–60% high relative humidity and (b) under 85 °C in a N₂ environment of MAPbI₃, MAPbI₃-IL, and MAPbI₃-IL/CQDs PSCs.

form a better energy-level alignment, which is beneficial for achieving efficient charge transport and collection. We attribute the improvement in energy-level alignment to the possible depolarization phenomenon that may occur after the introduction of CQDs, which changes the dipole effect on the surface of the film.^{57,58}

To investigate the stability of PSCs, we first test the stability performance of nonencapsulated devices at room temperature with RH of 50–60%. As shown in Figure 8a, the stability of MAPbI₃-IL/CQDs PSCs also dramatically improved and only a slight decay of less than 9% was found after 1600 h, which is significantly superior to that of the 80% decay of MAPbI₃ PSCs. The presence of the F element on the surface of the films is the primary reason for the significant enhancement in humidity stability,^{59,60} which increases the water contact angle and hinders the decomposition of perovskite by water molecules (Figures S14 and S15). Meanwhile, the MAPbI₃-IL/CQDs PSCs also showed the best stability in N₂ and 85 °C environments (Figure 8b). Due to the sensitivity of grain boundaries in perovskite films to thermal stress and their function as high-speed pathways for atomic, ionic, and molecular diffusion, the degradation of perovskites primarily propagates along the weakest grain boundaries in the films.^{61–64} Therefore, the MAPbI₃-IL/CQDs PSCs exhibit better thermal stability than MAPbI₃ PSCs and MAPbI₃-IL PSCs due to the high-quality perovskite films and the multipinning defect effects.

4. CONCLUSIONS

Separately introducing small amounts of BMIMBF₄ and CQDs to the perovskite precursor and antisolvent has been proven to be an effective simple approach for improving the crystallization of perovskite films and enhancing the photovoltaic performance of PSCs. Even though BMIMBF₄ can inhibit ion migration in the films and improve the stability of the PSCs. However, the large molecular ionic liquid BMIMBF₄ forms low-dimensional complexes with lead iodide, increasing steric hindrance and generating energy levels that do not match the functional layer, hindering charge carrier transfer and leading to decreased J_{sc} in the device. Carbon quantum dots, as highly conductive inorganic materials, contribute to passivating grain boundaries and promoting charge carrier transfer. By optimizing the content of CQDs and BMIMBF₄ additives, a synergistic effect of dual passivation of defects and promotion of charge carrier transport can be achieved in devices, resulting in a maximum efficiency of 20.84% in n-i-p MAPbI₃-based PSCs. The simplified manufacturing process provides a

straightforward method for improving the efficiency and stability of perovskite solar cells.

■ ASSOCIATED CONTENT

Supporting Information

The Supporting Information is available free of charge at <https://pubs.acs.org/doi/10.1021/acsami.3c11370>.

Device fabrication; scheme and characterization of CQDs; crystallization quality and defect passivation of MAPbI₃; MAPbI₃-IL and MAPbI₃-IL/CQDs; key J - V and photovoltaic parameters of PSCs; fitted EIS and TRPL parameters; and representative MAPbI₃-IL PSCs statistics table (PDF)

■ AUTHOR INFORMATION

Corresponding Authors

Jinghai Yang – Key Laboratory of Functional Materials Physics and Chemistry of the Ministry of Education, Jilin Normal University, Changchun 130103, P. R. China; orcid.org/0000-0001-8409-6035; Email: jhyang1@jlnu.edu.cn

Lili Yang – Key Laboratory of Functional Materials Physics and Chemistry of the Ministry of Education, Jilin Normal University, Changchun 130103, P. R. China; orcid.org/0000-0003-0333-1684; Email: llyang1980@126.com

Authors

Shaohua Chi – Changchun Institute of Optics, Fine Mechanics and Physics, Chinese Academy of Sciences, Changchun 130033, P. R. China; University of Chinese Academy of Sciences, Beijing 100049, P. R. China; Key Laboratory of Functional Materials Physics and Chemistry of the Ministry of Education, Jilin Normal University, Changchun 130103, P. R. China

Shuo Yang – College of Science, Changchun University, Changchun 130022, P. R. China

Yijie Wang – Key Laboratory of Functional Materials Physics and Chemistry of the Ministry of Education, Jilin Normal University, Changchun 130103, P. R. China

Dan Li – Key Laboratory of Functional Materials Physics and Chemistry of the Ministry of Education, Jilin Normal University, Changchun 130103, P. R. China

Le Zhang – Key Laboratory of Functional Materials Physics and Chemistry of the Ministry of Education, Jilin Normal University, Changchun 130103, P. R. China

Lin Fan – Key Laboratory of Functional Materials Physics and Chemistry of the Ministry of Education, Jilin Normal

University, Changchun 130103, P. R. China; orcid.org/0000-0001-6580-0867

Fengyou Wang – Key Laboratory of Functional Materials Physics and Chemistry of the Ministry of Education, Jilin Normal University, Changchun 130103, P. R. China; orcid.org/0000-0003-2146-849X

Xiaoyan Liu – Key Laboratory of Functional Materials Physics and Chemistry of the Ministry of Education, Jilin Normal University, Changchun 130103, P. R. China

Huilian Liu – Key Laboratory of Functional Materials Physics and Chemistry of the Ministry of Education, Jilin Normal University, Changchun 130103, P. R. China

Maobin Wei – Key Laboratory of Functional Materials Physics and Chemistry of the Ministry of Education, Jilin Normal University, Changchun 130103, P. R. China

Complete contact information is available at:
<https://pubs.acs.org/10.1021/acsami.3c11370>

Notes

The authors declare no competing financial interest.

ACKNOWLEDGMENTS

This work was supported by the National Natural Science Foundation of China [2207510 and 62275101] and the Program for the development of Science and Technology of Jilin province [20210509050RQ, YDZJ202201ZYTS300, and YDZJ202301ZYTS244].

REFERENCES

- (1) Liu, Y.; Xiang, W.; Mou, S.; Zhang, H.; Liu, S. Synergetic Surface Defect Passivation towards Efficient and Stable Inorganic Perovskite Solar Cells. *Chem. Eng. J.* **2022**, *447*, 137515–137524.
- (2) Yao, K.; Li, S.; Liu, Z.; Ying, Y.; Dvorak, P.; Fei, L.; Sikola, T.; Huang, H.; Nordlander, P.; Jen, A. K.; Lei, D. Plasmon-induced Trap Filling at Grain boundaries in Perovskite Solar Cells. *Light: Sci. Appl.* **2021**, *10*, No. 219, DOI: [10.1038/s41377-021-00662-y](https://doi.org/10.1038/s41377-021-00662-y).
- (3) Qing, J.; Liu, X.-K.; Li, M.; Liu, F.; Yuan, Z.; Tiukalova, E.; Yan, Z.; Duchamp, M.; Chen, S.; Wang, Y.; Bai, S.; Liu, J.-M.; Snaith, H. J.; Lee, C.-S.; Sum, T. C.; Gao, F. Aligned and Graded Type-II Ruddlesden-Popper Perovskite Films for Efficient Solar Cells. *Adv. Energy Mater.* **2018**, *8*, No. 1800185, DOI: [10.1002/aenm.201800185](https://doi.org/10.1002/aenm.201800185).
- (4) Zhang, Y.; Chen, M.; Zhou, Y.; Li, W.; Lee, Y.; Kanda, H.; Gao, X. X.; Hu, R.; Brooks, K. G.; Zia, R.; Kinge, S.; Padture, N. P.; Nazeeruddin, M. K. The Synergism of DMSO and Diethyl Ether for Highly Reproducible and Efficient MA_{0.5}FA_{0.5}PbI₃ Perovskite Solar Cells. *Adv. Energy Mater.* **2020**, *10*, No. 2001300, DOI: [10.1002/aenm.202001300](https://doi.org/10.1002/aenm.202001300).
- (5) Li, J.; Meng, X.; Wu, Z.; Duan, Y.; Guo, R.; Xiao, W.; Zhang, Y.; Li, Y.; Shen, Y.; Zhang, W.; Shao, G. Pinning Bromide Ion with Ionic Liquid in Lead-Free Cs₂AgBiBr₆ Double Perovskite Solar Cells. *Adv. Funct. Mater.* **2022**, *32*, No. 2112991, DOI: [10.1002/adfm.202112991](https://doi.org/10.1002/adfm.202112991).
- (6) Li, Y.; Fan, D.; Xu, F.; Shan, C.; Yu, J.; Li, W.; Luo, D.; Sun, Z.; Fan, H.; Zhao, M.; Li, X.; Cui, K.; Chen, R.; Li, G.; Kyaw, A. K. K. 1 + 1 > 2: Dual Strategies of Quinolinic cid Passivation and DMF Solvent Annealing for High-Performance Inverted Perovskite Solar Cell. *Chem. Eng. J.* **2022**, *435*, No. 135107, DOI: [10.1016/j.cej.2022.135107](https://doi.org/10.1016/j.cej.2022.135107).
- (7) Gao, X.-X.; Ding, B.; Kanda, H.; Fei, Z.; Luo, W.; Zhang, Y.; Shibayama, N.; Züttel, A.; Tirani, F. F.; Scopelliti, R.; Kinge, S.; Zhang, B.; Feng, Y.; Dyson, P. J.; Nazeeruddin, M. K. Engineering Long-Term Stability into Perovskite Solar Cells via Application of a Multi-Functional TFSI-Based Ionic Liquid. *Cell Rep. Phys. Sci.* **2021**, *2*, No. 100475, DOI: [10.1016/j.xcrp.2021.100475](https://doi.org/10.1016/j.xcrp.2021.100475).
- (8) Luo, M.; Zong, X.; Zhao, M.; Sun, Z.; Chen, Y.; Liang, M.; Wu, Y.; Xue, S. Synergistic Effect of Amide and Fluorine of Polymers Assist Stable Inverted Perovskite Solar Cells with Fill Factor > 83%. *Chem. Eng. J.* **2022**, *442*, No. 136136, DOI: [10.1016/j.cej.2022.136136](https://doi.org/10.1016/j.cej.2022.136136).
- (9) Yang, J.; Sheng, W.; Li, R.; Gong, L.; Li, Y.; Tan, L.; Lin, Q.; Chen, Y. Uncovering the Mechanism of Poly(Ionic-Liquid)s Multiple Inhibition of Ion Migration for Efficient and Stable Perovskite Solar Cells. *Adv. Energy Mater.* **2022**, *12*, No. 2103652, DOI: [10.1002/aenm.202103652](https://doi.org/10.1002/aenm.202103652).
- (10) Hatamvand, M.; Gholipour, S.; Chen, M.; Zhou, Y.; Jiang, T.; Hu, Z.; Chen, Y.; Huang, W. Dual-Side Interfacial Passivation of FAPbI₃ Perovskite Film By Naphthylmethylammonium Iodide for Highly Efficient and Stable Perovskite Solar Cells. *Chem. Eng. J.* **2023**, *460*, No. 141788, DOI: [10.1016/j.cej.2023.141788](https://doi.org/10.1016/j.cej.2023.141788).
- (11) Eames, C.; Frost, J. M.; Barnes, P. R.; O'Regan, B. C.; Walsh, A.; Islam, M. S. Ionic Transport in Hybrid Lead Iodide Perovskite Solar Cells. *Nat. Commun.* **2015**, *6*, No. 7497, DOI: [10.1038/ncomms8497](https://doi.org/10.1038/ncomms8497).
- (12) Saki, Z.; Byranvand, M. M.; Taghavinia, N.; Kedia, M.; Saliba, M. Solution-Processed Perovskite Thin-Films: the Journey From Lab-To Large-Scale Solar Cells. *Energy Environ. Sci.* **2021**, *14*, 5690–5722.
- (13) Ren, X.; Zhang, L.; Yuan, Y.; Ding, L. Ion Migration in Perovskite Solar Cells. *J. Semicond.* **2021**, *42*, No. 010201, DOI: [10.1088/1674-4926/42/1/010201](https://doi.org/10.1088/1674-4926/42/1/010201).
- (14) Hui, W.; Chao, L. F.; Lu, H.; Xia, F.; Wei, Q.; Su, Z. H.; Niu, T. T.; Tao, L.; Du, B.; Li, D. L.; Wang, Y.; Dong, H.; Zuo, S. W.; Li, B. X.; Shi, W.; Ran, X. Q.; Li, P.; Zhang, H.; Wu, Z. B.; Ran, C. X.; Song, L.; Xing, G. C.; Gao, X. Y.; Zhang, J.; Xia, Y. D.; Chen, Y. H.; Huang, W. Stabilizing Black-Phase Formamidinium Perovskite Formation at Room Temperature and High Humidity. *Science* **2021**, *371*, 1359–1364.
- (15) Zhang, X. L.; Huang, H. H.; Jin, L. J.; Wen, C.; Zhao, Q.; Zhao, C. Y.; Guo, J. J.; Cheng, C.; Wang, H. S.; Zhang, L.; Li, Y. Y.; Maung, Y. M.; Yuan, J. Y.; Ma, W. L. Ligand-Assisted Coupling Manipulation for Efficient and Stable FAPbI₃ Colloidal Quantum Dot Solar Cells. *Angew. Chem., Int. Ed.* **2022**, *62*, No. e202214241, DOI: [10.1002/anie.202214241](https://doi.org/10.1002/anie.202214241).
- (16) Deng, X. Y.; Xie, L. S.; Wang, S. R.; Li, C. B.; Wang, A. L.; Yuan, Y.; Cao, Z. Y.; Li, T. S.; Ding, L. M.; Hao, F. Ionic liquids Engineering for High-Efficiency and Stable Perovskite Solar Cells. *Chem. Eng. J.* **2020**, *398*, No. 122594, DOI: [10.1016/j.cej.2020.122594](https://doi.org/10.1016/j.cej.2020.122594).
- (17) Wang, A.; Wang, J.; Niu, X.; Zuo, C.; Hao, F.; Ding, L. Inhibiting Octahedral Tilting for Stable CsPbI₂Br Solar Cells. *InfoMat* **2022**, *4*, No. e12270, DOI: [10.1002/inf2.12263](https://doi.org/10.1002/inf2.12263).
- (18) Bai, S.; Da, P.; Li, C.; Wang, Z.; Yuan, Z.; Fu, F.; Kawecki, M.; Liu, X.; Sakai, N.; Wang, J. T.; Huettner, S.; Buecheler, S.; Fahlman, M.; Gao, F.; Snaith, H. J. Planar Perovskite Solar Cells with Long-Term Stability Using Ionic Liquid Additives. *Nature* **2019**, *571*, 245–250.
- (19) Calìò, L.; Salado, M.; Kazim, S.; Ahmad, S. A Generic Route of Hydrophobic Doping in Hole Transporting Material to Increase Longevity of Perovskite Solar Cells. *Joule* **2018**, *2*, 1800–1815.
- (20) Liang, C.; Gu, H.; Xia, Y.; Wang, Z.; Liu, X.; Xia, J.; Zuo, S.; Hu, Y.; Gao, X.; Hui, W.; Chao, L.; Niu, T.; Fang, M.; Lu, H.; Dong, H.; Yu, H.; Chen, S.; Ran, X.; Song, L.; Li, B.; Zhang, J.; Peng, Y.; Shao, G.; Wang, J.; Chen, Y.; Xing, G.; Huang, W. Two-Dimensional Ruddlesden–Popper Layered Perovskite Solar Cells Based on Phase-Pure Thin Films. *Nat. Energy* **2021**, *6*, 38–45.
- (21) Zhu, X. J.; Wang, C. Y.; Zhang, C.; Wang, Z. Y.; Feng, J. S.; Liu, S. Z.; Yang, D. Imidazolium-Based Ionic Liquid for Stable and Highly Efficient Black-Phase Formamidinium-Based Perovskite Solar. *Cell Chem. Eng. J.* **2022**, *434*, No. 134759, DOI: [10.1016/j.cej.2022.134759](https://doi.org/10.1016/j.cej.2022.134759).
- (22) Luo, Y.; Kong, L. M.; Wang, L.; Shi, X. Y.; Yuan, H.; Li, W. Q.; Wang, S.; Zhang, Z. J.; Zhu, W. Q.; Yang, X. Y. a Multifunctional Ionic Liquid Additive Enabling Stable and Efficient Perovskite Light-

Emitting Diodes. *Small* **2022**, *18*, No. 2200498, DOI: 10.1002/smll.202200498.

(23) Zhang, Y.; Fei, Z.; Gao, P.; Lee, Y.; Tirani, F. F.; Scopelliti, R.; Feng, Y.; Dyson, P. J.; Nazeeruddin, M. K. A Strategy to Produce High Efficiency, High Stability Perovskite Solar Cells Using Functionalized Ionic Liquid-Dopants. *Adv. Mater.* **2017**, *29*, No. 1702157, DOI: 10.1002/adma.201702157.

(24) Zhang, L.; Mei, L.; Wang, K.; Lv, Y.; Zhang, S.; Lian, Y.; Liu, X.; Ma, Z.; Xiao, G.; Liu, Q.; Zhai, S.; Zhang, S.; Liu, G.; Yuan, L.; Guo, B.; Chen, Z.; Wei, K.; Liu, A.; Yue, S.; Niu, G.; Pan, X.; Sun, J.; Hua, Y.; Wu, W.-Q.; Di, D.; Zhao, B.; Tian, J.; Wang, Z.; Yang, Y.; Chu, L.; Yuan, M.; Zeng, H.; Yip, H.-L.; Yan, K.; Xu, W.; Zhu, L.; Zhang, W.; Xing, G.; Gao, F.; Ding, L. Advances in the Application of Perovskite Materials. *Nano-Micro Lett.* **2023**, *15*, No. 177, DOI: 10.1007/s40820-023-01140-3.

(25) Wang, A.; Deng, X.; Wang, J.; Wang, S.; Niu, X.; Hao, F.; Ding, L. Ionic Liquid Reducing Energy Loss and Stabilizing CsPbI₃Br Solar Cells. *Nano Energy* **2021**, *81*, No. 105631, DOI: 10.1016/j.nanoen.2020.105631.

(26) Wang, S.; Li, Z.; Zhang, Y.; Liu, X.; Han, J.; Li, X.; Liu, Z.; Liu, S.; Choy, W. C. H. Water-Soluble Triazolium Ionic-Liquid-Induced Surface Self-Assembly to Enhance the Stability and Efficiency of Perovskite Solar Cells. *Adv. Funct. Mater.* **2019**, *29*, No. 1900417, DOI: 10.1002/adfm.201900417.

(27) Akin, S.; Akman, E.; Sonmezoglu, S. FAPbI₃-Based Perovskite Solar Cells Employing Hexyl-Based Ionic Liquid with an Efficiency Over 20% and Excellent Long-Term Stability. *Adv. Funct. Mater.* **2020**, *30*, No. 2002964, DOI: 10.1002/adfm.202002964.

(28) Fang, M.; Tao, L.; Wu, W.; Wei, Q.; Xia, Y. D.; Li, P.; Ran, X. Q.; Zhong, Q.; Xing, G. C.; Song, L.; Muller-Buschbaum, P.; Zhang, H.; Chen, Y. H. Residual Solvent Extraction via Chemical Displacement for Efficient and Stable Perovskite Solar Cells. *J. Energy Chem.* **2021**, *61*, 8–14.

(29) Pandey, S.; Karakoti, M.; Bhardwaj, D.; Tatrari, G.; Sharma, R.; Pandey, L.; Lee, M. J.; Sahoo, N. G. Recent Advances in Carbon-Based Materials for High-Performance Perovskite Solar Cells: Gaps, Challenges and Fulfillment. *Nanoscale Adv.* **2023**, *5*, 1492–1526.

(30) Hadadian, M.; Smatt, J. H.; Correa-Baena, J. P. The Role of Carbon-Based Materials in Enhancing the Stability of Perovskite Solar Cells. *Energy Environ. Sci.* **2020**, *13*, 1377–1407.

(31) You, P.; Tang, G.; Cao, J.; Shen, D.; Ng, T. W.; Hawash, Z.; Wang, N.; Liu, C. K.; Lu, W.; Tai, Q.; Qi, Y.; Lee, C. S.; Yan, F. 2D Materials for Conducting Holes From Grain Boundaries in Perovskite Solar Cells. *Light: Sci. Appl.* **2021**, *10*, 68–79.

(32) Mirtchev, P.; Henderson, E. J.; Soheilnia, N.; Yip, C. M.; Ozin, G. A. Solution Phase Synthesis of Carbon Quantum Dots as Sensitizers for Nanocrystalline TiO₂ Solar Cells. *J. Mater. Chem.* **2012**, *22*, 1265–1269.

(33) Baker, S. N.; Baker, G. A. Luminescent Carbon Nanodots: Emergent Nanolights. *Angew. Chem., Int. Ed.* **2010**, *49*, 6726–6744.

(34) Molaie, M. J. The Optical Properties and Solar Energy Conversion Applications of Carbon Quantum Dots: A review. *Sol. Energy* **2020**, *196*, 549–566.

(35) Xie, S.; Su, H.; Wei, W.; Li, M.; Tong, Y.; Mao, Z. Remarkable Photoelectrochemical Performance of Carbon Dots Sensitized TiO₂ Under Visible Light Irradiation. *J. Mater. Chem. A* **2014**, *2*, 16365–16368.

(36) Dou, X.; Lin, Z.; Chen, H.; Zheng, Y.; Lu, C.; Lin, J.-M. Production of Superoxide Anion Radicals as Evidence for Carbon Nanodots Acting as Electron Donors By the Chemiluminescence Method. *ChemComm* **2013**, *49*, 5871–5873.

(37) Ghosh, T.; Chatterjee, S.; Prasad, E. Photoinduced Electron Transfer from Various Aniline Derivatives to Graphene Quantum Dots. *J. Phys. Chem. A* **2015**, *119*, 11783–11790.

(38) Guo, Q.; Yuan, F.; Zhang, B.; Zhou, S.; Zhang, J.; Bai, Y.; Fan, L.; Hayat, T.; Alsaedi, A.; Tan, Z. Passivation of the Grain Boundaries of CH₃NH₃PbI₃ Using Carbon Quantum Dots for Highly Efficient Perovskite Solar Cells with Excellent Environmental Stability. *Nanoscale* **2019**, *11*, 115–124.

(39) Ma, Y.; Zhang, H.; Zhang, Y.; Hu, R.; Jiang, M.; Zhang, R.; Lv, H.; Tian, J.; Chu, L.; Zhang, J.; Xue, Q.; Yip, H. L.; Xia, R.; Li, X.; Huang, W. Enhancing the Performance of Inverted Perovskite Solar Cells via Grain Boundary Passivation with Carbon Quantum Dots. *ACS Appl. Mater. Interfaces* **2019**, *11*, 3044–3052.

(40) Zhang, W.; Du, J.; Qiu, C.; Yang, K.; Huang, Q.; Wang, Q.; Zhang, W.; Han, H.; Gao, X.; Hu, Y. Enhanced Efficiency of Printable Mesoscopic Perovskite Solar Cells Using Ionic Liquid Additives. *Chem. Commun.* **2021**, *57*, 4027–4030.

(41) Xia, R.; Gao, X. X.; Zhang, Y.; Drigo, N.; Queloz, V. I. E.; Tirani, F. F.; Scopelliti, R.; Huang, Z.; Fang, X.; Kinge, S.; Fei, Z.; Roldan-Carmona, C.; Nazeeruddin, M. K.; Dyson, P. J. An Efficient Approach to Fabricate Air-Stable Perovskite Solar Cells via Addition of a Self-Polymerizing Ionic Liquid. *Adv. Mater.* **2020**, *32*, No. 2003801, DOI: 10.1002/adma.202003801.

(42) Kim, H.; Lee, J. W.; Han, G. R.; Kim, S. K.; Oh, J. H. Synergistic Effects of Cation and Anion in an Ionic Imidazolium Tetrafluoroborate Additive for Improving the Efficiency and Stability of Half-Mixed Pb-Sn Perovskite Solar Cells. *Adv. Funct. Mater.* **2021**, *31*, No. 2008801, DOI: 10.1002/adfm.202008801.

(43) Chen, J.; Rong, Y.; Mei, A.; Xiong, Y.; Liu, T.; Sheng, Y.; Jiang, P.; Hong, L.; Guan, Y.; Zhu, X.; Hou, X.; Duan, M.; Zhao, J.; Li, X.; Han, H. Hole-Conductor-Free Fully Printable Mesoscopic Solar Cell with Mixed-Anion Perovskite CH₃NH₃PbI_(3-x)(BF₄)_x. *Adv. Energy Mater.* **2016**, *6*, No. 1502009, DOI: 10.1002/aenm.201502009.

(44) Zhuang, X. M.; Chen, X. F.; Xu, L.; Liu, S. A.; Wu, Y. J.; Shi, Z. C.; Zhou, Q. Q.; Li, B.; Yan, H. X.; Reiss, P.; Song, H. W. Halide Anions Engineered Ionic Liquids Passivation Layer for Highly Stable Inverted Perovskite Solar Cells. *J. Colloid Interface Sci.* **2022**, *622*, 469–480.

(45) Suo, J.; Yang, B.; Mosconi, E.; Choi, H. S.; Kim, Y.; Zakeeruddin, S. M.; De Angelis, F.; Grätzel, M.; Kim, H. S.; Hagfeldt, A. Surface Reconstruction Engineering with Synergistic Effect of Mixed-Salt Passivation Treatment toward Efficient and Stable Perovskite Solar Cells. *Adv. Funct. Mater.* **2021**, *31*, No. 2102902, DOI: 10.1002/adfm.202102902.

(46) Duan, C.; Cao, J.; Liang, Z.; Ming, Y.; Li, J.; Zhao, L.; Dong, B.; Li, J.; Wu, C.; Wang, S. Ionic Liquid Additive-Assisted Highly Efficient Electron Transport Layer-Free Perovskite Solar Cells. *Sol. RRL* **2021**, *5*, No. 2100648, DOI: 10.1002/solr.202100648.

(47) Chen, P.; Zhang, Y.; Du, J.; Wang, Y.; Zhang, X.; Liu, Y. Global Control of CH₃NH₃PbI₃ Formation with Multifunctional Ionic Liquid for Perovskite Hybrid Photovoltaics. *J. Phys. Chem. C* **2018**, *122*, 10699–10705.

(48) Yang, J.; Sheng, W.; Li, R.; Gong, L.; Li, Y.; Tan, L.; Lin, Q.; Chen, Y. Uncovering the Mechanism of Poly(Ionic-Liquid)s Multiple Inhibition of Ion Migration for Efficient and Stable Perovskite Solar Cells. *Adv. Energy Mater.* **2022**, *12*, No. 2103652, DOI: 10.1002/aenm.202103652.

(49) Zhou, L.; Su, J.; Lin, Z.; Guo, X.; Ma, J.; Li, T.; Zhang, J.; Chang, J.; Hao, Y. Synergistic Interface Layer Optimization and Surface Passivation with Fluorocarbon Molecules toward Efficient and Stable Inverted Planar Perovskite Solar. *Cells Res.* **2021**, *2021*, No. 9836752, DOI: 10.34133/2021/9836752.

(50) Xia, X.; Peng, J.; Wan, Q.; Wang, X.; Fan, Z.; Zhao, J.; Li, F. Functionalized Ionic Liquid-Crystal Additive for Perovskite Solar Cells with High Efficiency and Excellent Moisture Stability. *ACS Appl. Mater. Interfaces* **2021**, *13*, 17677–17689.

(51) Zhou, Z.; Lian, H. J.; Xie, J.; Qiao, W. C.; Wu, X. F.; Shi, Y.; Wang, X. L.; Dai, S.; Yuan, H.; Hou, Y.; Yang, S.; Yang, H. G. Non-Selective Adsorption of Organic Cations Enables Conformal Surface Capping of Perovskite Grains for Stabilized Photovoltaic Operation. *Cell Rep. Phys. Sci.* **2022**, *3*, No. 100760, DOI: 10.1016/j.xcrp.2022.100760.

(52) Lv, Y.; Zhang, H.; Wang, J.; Chen, L.; Bian, L.; An, Z.; Qian, Z.; Ren, G.; Wu, J.; Nuesch, F.; Huang, W. All-In-One Deposition to Synergistically Manipulate Perovskite Growth for High-Performance Solar Cell. *Research* **2020**, *2020*, No. 2763409, DOI: 10.34133/2020/2763409.

(53) Du, Y.; Tian, Q.; Chang, X.; Fang, J.; Gu, X.; He, X.; Ren, X.; Zhao, K.; Liu, S. Ionic Liquid Treatment for Highest-Efficiency Ambient Printed Stable All-Inorganic CsPbI₃ Perovskite Solar Cells. *Adv. Mater.* **2022**, *34*, No. 2106750, DOI: 10.1002/adma.202106750.

(54) Li, Y.; Chen, Z.; Yu, B.; Tan, S.; Cui, Y.; Wu, H.; Luo, Y.; Shi, J.; Li, D.; Meng, Q. Efficient Stable Formamidinium-Cesium Perovskite Solar Cells and Minimodules Enabled by Crystallization Regulation. *Joule* **2022**, *6*, 676–689, DOI: 10.1016/j.joule.2022.02.003.

(55) Liang, Z.; Xu, H.; Zhang, Y.; Liu, G.; Chu, S.; Tao, Y.; Xu, X.; Xu, S.; Zhang, L.; Chen, X.; Xu, B.; Xiao, Z.; Pan, X.; Ye, J. Selective Targeting Anchor Strategy Afford Efficient and Stable Ideal Bandgap Perovskite Solar Cells. *Adv. Mater.* **2022**, *34*, No. 2110241, DOI: 10.1002/adma.202110241.

(56) Zhu, H.; Ren, Y.; Pan, L.; Ouellette, O.; Eickemeyer, F. T.; Wu, Y.; Li, X.; Wang, S.; Liu, H.; Dong, X.; Zakeeruddin, S. M.; Liu, Y.; Hagfeldt, A.; Gratzel, M. Synergistic Effect of Fluorinated Passivator and Hole Transport Dopant Enables Stable Perovskite Solar Cells with an Efficiency Near 24%. *J. Am. Chem. Soc.* **2021**, *143*, 3231–3237.

(57) Zhou, Q.; Cai, C.; Xiong, Q.; Zhang, Z.; Xu, J.; Liang, L.; Wang, S.; Sun, W.; Yuan, Z.; Gao, P. Surface Polarity Regulation by Relieving Fermi-Level Pinning with Naphthalocyanine Tetraimides toward Efficient Perovskite Solar Cells with Improved Photostability. *Adv. Energy Mater.* **2022**, *12*, No. 2201243, DOI: 10.1002/aenm.202201243.

(58) Canil, L.; Cramer, T.; Fraboni, B.; Ricciarelli, D.; Meggiolaro, D.; Singh, A.; Liu, M.; Rusu, M.; Wolff, C. M.; Phung, N.; Wang, Q.; Neher, D.; Unold, T.; Vivo, P.; Gagliardi, A.; De Angelis, F.; Abate, A. Tuning Halide Perovskite Energy Levels. *Energy Environ. Sci.* **2021**, *14*, 1429–1438.

(59) Kahn, A. Fermi level, Work Function and Vacuum Level. *Mater. Horiz.* **2016**, *3*, 7–10.

(60) Li, M.; Zhao, C.; Wang, Z. K.; Zhang, C. C.; Lee, H. K. H.; Pockett, A.; Barbé, J.; Tsoi, W. C.; Yang, Y. G.; Carnie, M. J.; Gao, X. Y.; Yang, W. X.; Durrant, J. R.; Liao, L. S.; Jain, S. M. Interface Modification by Ionic Liquid: A Promising Candidate for Indoor Light Harvesting and Stability Improvement of Planar Perovskite Solar Cells. *Adv. Energy Mater.* **2018**, *8*, No. 1801509, DOI: 10.1002/aenm.201801509.

(61) Zhou, X.; Wang, Y. Y.; Li, C. Y.; Wu, T. Doping Amino-Functionalized Ionic Liquid in Perovskite Crystal for Enhancing Performances of Hole-Conductor Free Solar Cells with Carbon Electrode. *Chem. Eng. J.* **2019**, *372*, 46–52.

(62) Siegler, T. D.; Dunlap-Shohl, W. A.; Meng, Y.; Yang, Y.; Kau, W. F.; Sunkari, P. P.; Tsai, C. E.; Armstrong, Z. J.; Chen, Y. C.; Beck, D. A. C.; Meila, M.; Hillhouse, H. W. Water-Accelerated Photo-oxidation of CH₃NH₃PbI₃ Perovskite. *J. Am. Chem. Soc.* **2022**, *144*, 5552–5561.

(63) Qin, T. X.; You, E. M.; Zhang, M. X.; Zheng, P.; Huang, X. F.; Ding, S. Y.; Mao, B. W.; Tian, Z. Q. Quantification of Electron Accumulation at Grain Boundaries in Perovskite Polycrystalline Films By Correlative Infrared-Spectroscopic Nanoimaging and Kelvin Probe Force Microscopy. *Light: Sci. Appl.* **2021**, *10*, 84–91.

(64) Jin, Z.; Peng, Y.; Fang, Y.; Ye, Z.; Fan, Z.; Liu, Z.; Bao, X.; Gao, H.; Ren, W.; Wu, J.; Ma, G.; Chen, Q.; Zhang, C.; Balakin, A. V.; Shkurinov, A. P.; Zhu, Y.; Zhuang, S. Photoinduced Large Polaron Transport and Dynamics in Organic-Inorganic Hybrid Lead Halide Perovskite with Terahertz Probes. *Light: Sci. Appl.* **2022**, *11*, 209–220.